A 22 GHz mobile microwave radiometer for the study of stratospheric water vapour

Erwan Motte, Philippe Ricaud, Benjamin Gabard, Mathieu Niclas, Fabrice Gangneron

▶ **To cite this version:**

Erwan Motte, Philippe Ricaud, Benjamin Gabard, Mathieu Niclas, Fabrice Gangneron. A 22 GHz mobile microwave radiometer for the study of stratospheric water vapour. Reunion Island International Conference, Nov 2007, La Réunion, France. 10.1109/TGRS.2008.2000626 . hal-00224825

HAL Id: hal-00224825
https://hal.science/hal-00224825

Submitted on 25 Oct 2021

HAL is a multi-disciplinary open access archive for the deposit and dissemination of scientific research documents, whether they are published or not. The documents may come from teaching and research institutions in France or abroad, or from public or private research centers.

L'archive ouverte pluridisciplinaire **HAL**, est destinée au dépôt et à la diffusion de documents scientifiques de niveau recherche, publiés ou non, émanant des établissements d'enseignement et de recherche français ou étrangers, des laboratoires publics ou privés.

Distributed under a Creative Commons Attribution 4.0 International License

A 22-GHz Mobile Microwave Radiometer (MobRa) for the Study of Middle Atmospheric Water Vapor

Erwan Motte, Philippe Ricaud, Benjamin Gabard, Mathieu Niclas, and Fabrice Gangneron

***Abstract*—We present a new compact and automated ground-based microwave mobile radiometer dedicated to the study of middle atmospheric water vapor, which is convenient for measurement, intercomparison, and validation campaigns, particularly in remote places. The instrument detects the $6_{16}-5_{23}$ H_2O transition line at 22.235 GHz by means of balanced beam-switching observation of the atmosphere. Tipping curves are performed to estimate the tropospheric opacity. The sky is used as a cold load for calibration, minimizing the use of liquid nitrogen. The main technical issues are caused by the small horn antenna (a beamwidth of $\sim 12^\circ$) inducing large bias when using pencil-beam approximation for the calculation of elevation-dependent parameters. Numerical methods have been developed to include this effect in the data calibration process. Preliminary vertical profiles are retrieved with the Microwave Odin LIne Estimation and REtrieval radiative transfer and inversion tool from 25 to 55 km with a vertical resolution of 10–20 km increasing with height, for an integration time of $\sim$12 h and a measurement error of $\sim 15\%$ ($\sim$0.8 ppmv). Preliminary comparisons with the spaceborne instrument Aura/Microwave Limb Sounder show a good agreement ($\sim 5\%$) in the 35–55-km altitude range, whereas a negative bias is detected below (up to -30% at 25 km).**

***Index Terms*—Atmospheric measurement, calibration, radiometry.**

I. Introduction

WATER vapor (H_2O) is a key constituent of the middle atmosphere. It plays a major role in the energy balance of the Earth's atmosphere by emitting and absorbing in the infrared domain. It also takes parts in several reactions involving ozone chemistry and in the formation of polar stratospheric clouds. In addition, owing to its long lifetime, H_2O can be used as a tracer of middle atmospheric dynamics. The concentration of middle atmospheric H_2O is governed by the oxidation of methane and by the direct injection from the troposphere, particularly in the tropics as the main sources, and photolysis through solar Lyman-α radiation as the main sink. Over the period from 1980 to 2000, an increase in stratospheric water vapor has been observed by means of radiosoundings [1] and confirmed by remote-sensing measurements [2]. Since 2001, a decrease in H_2O has been measured [3], whereas a recent reprocessing of *in situ* data minimizes the previously measured trends [4].

The authors are with the Laboratoire d'Aérologie, Université de Toulouse, Centre National de la Recherche Scientifique UMR 5560, 31400 Toulouse, France (e-mail: erwan.motte@aero.obs-mip.fr).

Some satellite instruments (e.g., Odin/Submillimeter Radiometer [5], Aura/Microwave Limb Sounder (MLS) [6], ENVISAT/Michelson Interferometer for Passive Atmospheric Sounding [7], and MetOp/Infrared Atmospheric Sounding Interferometer [8]) measure H_2O in the stratosphere and/or in the troposphere and need ground-based measurements for validation.

The first ground-based measurements of middle atmospheric water vapor by observation of the $6_{16}-5_{23}$ H_2O transition line at 22.235 GHz with microwave radiometers were performed in the late 1970s [9]. Since then, new measurement methods improving calibration and stability have been developed [10], [11]. For more than 20 years, the technology has been evolving, instrumental noise level has been drastically reduced, even with uncooled amplifiers, and spectrometers have increased in bandwidth and resolution. Nevertheless, relatively few ground-based instruments exist at present, which are mainly located in the mid- or high-latitude regions, e.g., Water Vapor Millimeter-Wave Spectrometer instruments in California (U.S.), New Zealand and Hawaii (U.S.) [12], Onsala Radiometer in Gothenburg, Sweden [13], Middle Atmospheric Water Vapor Radiometer in Bern, Switzerland [14], and Radiometer for Atmospheric Measurements in Spitsbergen, Norway [15]. Most of them belong to the international Network for the Detection of Atmospheric Composition Change (NDACC) [16].

We present a new compact and automated ground-based radiometer for the study of middle atmospheric water vapor. Nowadays, microwave mobile radiometer (MobRa) is the most compact and transportable instrument for measuring middle atmospheric H_2O. It uses a new technique for the calibration of elevation, and new analysis methods have been set up to account for its large beamwidth. Its home base is located at Lannemezan Atmospheric Research Center, France [43° N, 0.2° E, and 580 m above sea level (a.s.l.)]. MobRa is also a prototype for developing two other instruments to be installed at the following: 1) at the Reunion Island Observatory on Maïdo summit (21° S, 55° E, and 2100 m a.s.l.) in the Indian Ocean and 2) at the Dome C Concordia station in Antarctica (75° S, 123° E, and 3200 m a.s.l.). The aim of this global project is to provide information about the long-term trends of water vapor at different latitudes in the scope of NDACC.

The first part of this paper will describe the instrumental setup (Section II) and the measurement and calibration principles (Section III) with a particular focus on the specific methods required to cope with the large beamwidth caused by the reduced antenna size (Section IV). The second part will deal with data analysis and retrievals (Section V) and will present preliminary results (Section V-C).

II. Instrument

A. Measurement Principle

The MobRa instrument measures the intensity of the H_2O microwave emission line at 22.235 GHz. The shape of this spectral line is governed mainly by two processes: 1) the temperature-dependent Doppler broadening and 2) the pressure-dependent collisional broadening [17]. In the atmosphere, as pressure decreases exponentially with height, the line shape is therefore related to the vertical distribution of the species. Inversion techniques can be used to retrieve vertical profiles from ground-based observations at only one observation angle. The maximum retrieval height is limited by the spectrometer resolution and the Doppler broadening effect to about 75–80 km at ∼22 GHz [17], whereas the minimum retrieval height is limited by the instrument total bandwidth and the so-called baseline ripples.

In microwave radiometry, the intensity of radiation is often expressed in terms of brightness temperature T_b, which is proportional to the physical temperature of a blackbody emitting in the Rayleigh–Jeans approximation of the Planck Law [17]. The observed brightness temperature $T_{\mathrm{b,out}}(\nu)$ at the location $s = s_\mathrm{out}$ of the line of sight can be approximated by the radiative transfer equation [18] as a function of initial brightness temperature $T_{\mathrm{b,in}}(\nu)$ at the location $s = s_\mathrm{in}$, the physical temperature of the medium, i.e., the atmosphere $T(s)$, and the absorption coefficient $\alpha(\nu, s)$ at the location s and frequency ν

$$T_{\mathrm{b,out}}(\nu) = T_{\mathrm{b,in}}(\nu) e^{-\tau(\nu, s_\mathrm{in})} + \int_{s_\mathrm{out}}^{s_\mathrm{in}} T(s) e^{-\tau(\nu,s)} \alpha(\nu, s) ds \quad (1)$$

where $\tau(\nu, s)$ is the optical depth or opacity defined as the integral of the absorption coefficient along the line of sight

$$\tau(\nu, s) = \int_0^s \alpha(\nu, s') ds'. \quad (2)$$

B. Description of the Instrument

The instrument is shown in Fig. 1, and the functional block diagram is shown in Fig. 2. It is a compact radiometer ($1 \times 1 \times 1.2$ m^3 and ∼100 kg), which was initially developed at the Laboratoire d'Astrodynamique, d'Astrophysique et d'Aéronomie de Bordeaux, France, and designed to be easily transported. The instrument has undergone several major changes in the previous years in order to implement new measurement techniques and to improve the quality and stability of the measured signal. The current receiver is composed of a Potter horn having a theoretical beamwidth of ∼12° full-width at half-maximum (FWHM), which is consistent with the simulated and measured antenna patterns (Fig. 3), followed by an uncooled low-noise high-electron mobility transistor amplifier exhibiting a noise figure of 1.5. The heterodyne single-side band (SSB) mixing stage downconverts the signal to the intermediate-frequency band of 1.6–2.5 GHz. SSB filtering is achieved after the first amplification stage by a bandpass cavity filter centered at 22.235 GHz and having a bandwidth of 1 GHz. Based on the vendor test sheets, the rejection in the image band is better than 32 dB ($< 0.1\%$). The total receiver noise temperature of the receiver T_rec is ∼200-K SSB, and the total front-end amplification is about 80 dB. The front end is in a temperature-controlled shielded enclosure. The signal is analyzed by an acousto-optical spectrometer (AOS) having an effective bandwidth of 850 MHz on 1600 channels and an Allan variance stability of 10 s. The AOS detection threshold is −64 dBm, and its response is linear up to −50-dBm input power. A frequency calibration is performed every two weeks by injecting a Dirac-comb signal of known frequencies into the spectrometer. Control and acquisition routines are operated from a standard PC running Labview. Note that, at the present time, MobRa still needs a human intervention to be covered in case of rain. An automated mechanical roof commanded by a rain sensor is currently being designed in order for MobRa to be fully automated.

Fig. 1. MobRa instrument for the measurement of middle atmospheric H_2O on the terrace of the Laboratoire d'Aérologie, Toulouse, France.

C. Measurement Method

1) Beam-Switching Method: The radiometer uses the balanced beam-switching method described in [10], i.e., measures the difference $[S - R]$ between a signal beam $[S]$ at low elevation, having a long pathlength in the atmosphere and a reference beam $[R]$ at high elevation. This method prevents the system from being sensitive to nonlinearities in the system gain and tropospheric opacity variations. In the present setup, $[S]$ has an elevation ranging from 20° to 35°, depending on the tropospheric conditions, and $[R]$ is directed toward zenith. A piece of microwave absorber ECCOSORB AN-74, which from hereon will be considered as the dielectric balance load, is inserted into the reference beam to compensate for the lower atmospheric emission. The signal beam $[S]$ elevation is automatically adjusted so that $[S - R]$ is close to zero.

2) Measurement Cycles and Calibration Scheme: Each $[S - R]$ measurement cycle takes about 1 min, including

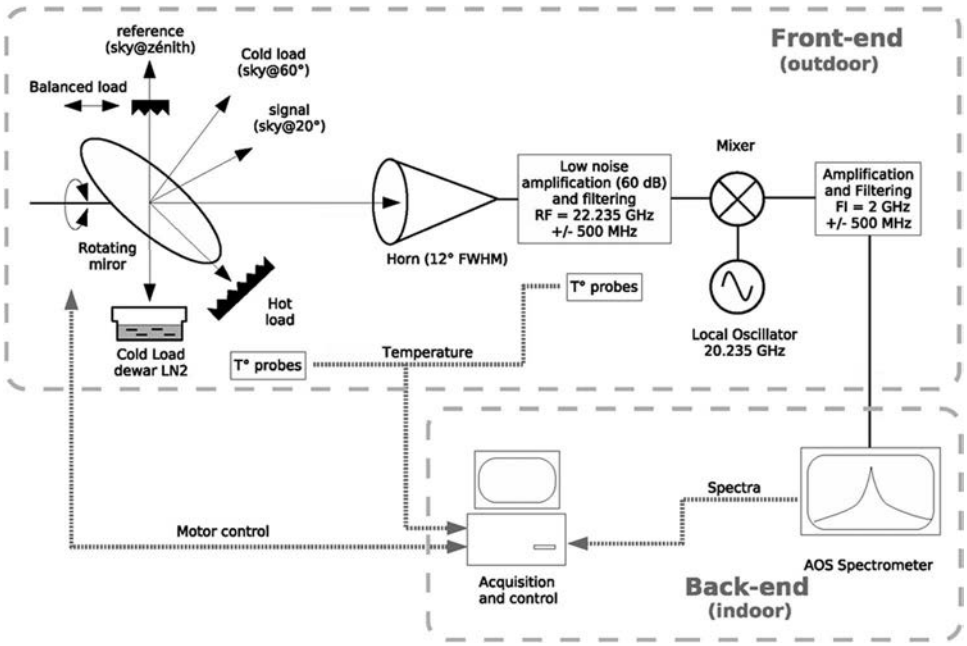

Fig. 2. H_2O MobRa instrument block diagram.

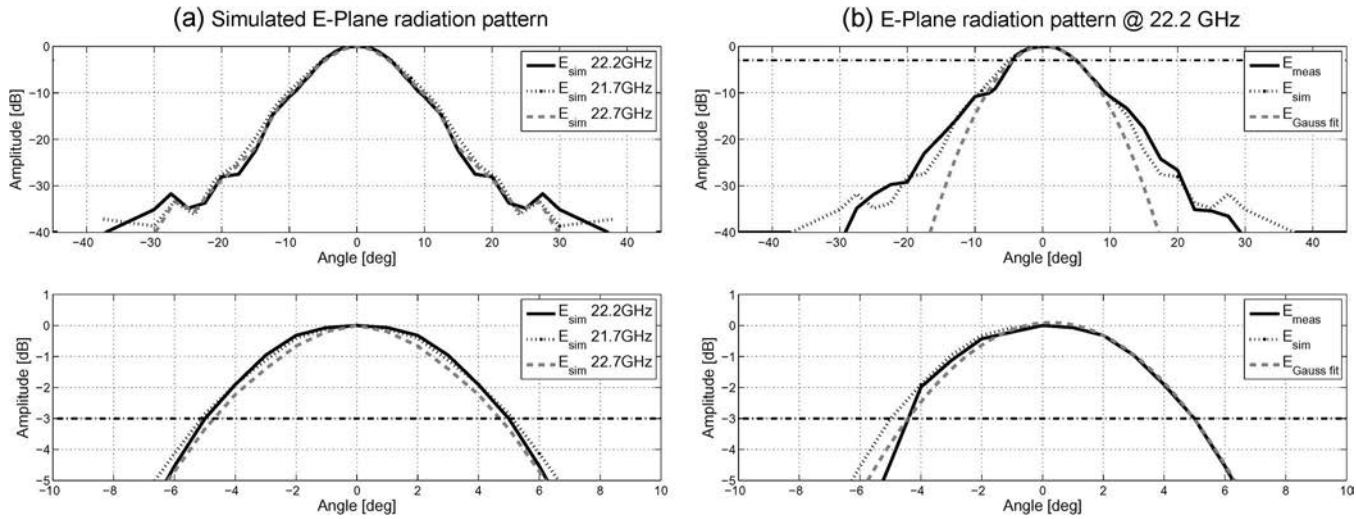

Fig. 3. Radiation patterns of the horn used by MobRa in the E-plane (vertical polarization). (a) Simulations for the center frequency, i.e., 22.2 GHz (solid line), and for the frequencies at the edge of the band, i.e., 21.7 (dotted line) and 22.7 GHz (dashed line). Top: Whole beam. Bottom: Zoom on the center of the beam. (b) Radiation patterns at 22.2 GHz: Measured (solid line), simulated (dotted line), and modeled by a Gaussian function (dashed line). As for (a), lower panel is a zoom on the center of the beam. The horizontal dash–dotted line represents the −3-dB level.

balancing, and corresponds to an effective integration time of about 10 s. In every 15 measurement cycles, a calibration cycle is performed during which several measurements are made. The so-called tipping curve (elevation scanning) is achieved in order to determine the properties of the troposphere followed by hot load (piece of HR1 microwave absorber at ambient temperature) and cold load (sky at 60° elevation) measurements. Liquid nitrogen (LN2) is also used as a cold load on a weekly basis in order to validate the usual calibration method. Calibration procedures will be detailed in Section III-A.

3) Calibration of Elevation: Even small errors in elevation angle value can induce large bias on signal intensity, particularly at low elevations. We used a sky scanning method to calibrate the elevation angle, which is based on the hypothesis that, in clear sky conditions, the instrument should measure the smallest intensity in the zenith direction, as the instrument is pointing toward the shortest atmospheric pathlength.

Our method consists of a clear sky scan at the elevation angle θ ranging from 45° to 90° on both sides of the zenith direction in the vertical measurement plane, which is by steps of 0.45° (five motor steps). Integration time is set to 150 ms per scan angle. The dielectric balance load and the hot load have to be removed for this operation. Data are then automatically analyzed. The derivative of the averaged power from channels 400 to 1000 (namely, from 22.05 to 22.50 GHz) versus the zenith angle is computed (Fig. 4). This derivative should be equal to zero when the received power versus angle reaches a minimum. In order to cope with the fluctuations coming from the instrumental noise,

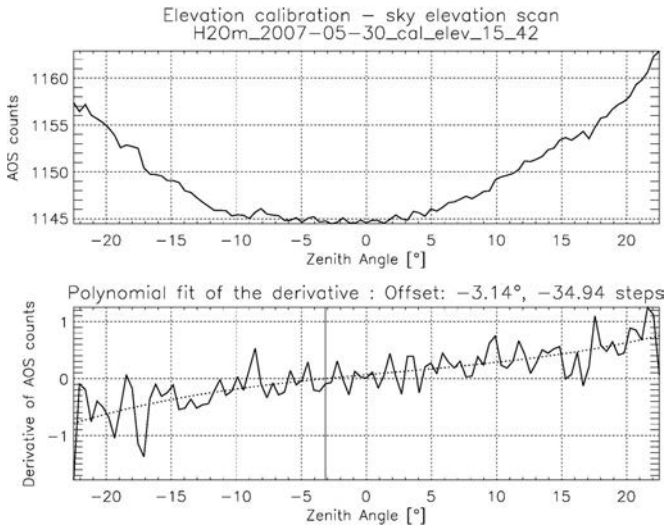

Fig. 4. Calibration of the mirror elevation, using the zenith-minimum technique. Upper panel: Measured total power versus mirror position. Lower panel: First derivative of the measured total power versus mirror position. The vertical line represents the estimated angular offset.

we fit a third-order polynomial function and compute the real root of the function, which corresponds to the elevation offset. Several elevation scans that are performed the same day show a variability within $\pm 0.5^\circ$. The main advantage of this method relies on its simplicity and is well suited for measurement campaigns. However, to achieve a better accuracy, particularly for long-term measurements, other calibration methods, e.g., sun scanning, are actually being investigated.

III. Raw Data Processing

A. Calibration

The antenna brightness temperature $T_{\rm a}(\nu)$ corresponding to the energy emitted by the atmosphere and coupled with the antenna is linked to the output of each channel of the spectrometer $V_{\rm a}(\nu)$ as

$$V_{\rm a}(\nu) = G(\nu)\left(T_{\rm a}(\nu) + T_{\rm rec}(\nu)\right) + V_0(\nu) \tag{3}$$

where $G(\nu)$ is the gain of the system, $V_0(\nu)$ is the spectrometer offset, or zero-check, and $T_{\rm rec}(\nu)$ is the receiver noise temperature. $V_0(\nu)$ can be easily measured by plugging a matched load to the input of the spectrometer. $G(\nu)$ and $T_{\rm rec}(\nu)$ can be calculated by pointing the instrument horn toward two targets (the so-called cold and hot loads) that are considered as black bodies with known physical temperatures [19].

The calibrated balanced spectrum $T_{\rm a}^{[S-R]}(\nu)$ is calculated from the spectrometer outputs $V_{\rm a}^{[S]}(\nu)$ and $V_{\rm a}^{[R]}(\nu)$ of the $[S]$ and $[R]$ measurements, respectively, using only $G(\nu)$, by considering $T_{\rm rec}(\nu)$ and $V_0(\nu)$ stable during the $[S]$ and $[R]$ measurements. From (3), $T_{\rm a}^{[S-R]}(\nu)$ can be estimated as

$$T_{\rm a}^{[S-R]}(\nu) = \left(V_{\rm a}^{[S]}(\nu) - V_{\rm a}^{[R]}(\nu)\right)/G(\nu). \tag{4}$$

As the calibration is performed only every 15 $[S-R]$ measurements, calibration information [$G(\nu)$ and $V_{\rm a}^{[\rm cold]}(\nu)$] is linearly interpolated for every $[S-R]$ measurement pair. We now drop the ν notation for the frequency-dependent variables.

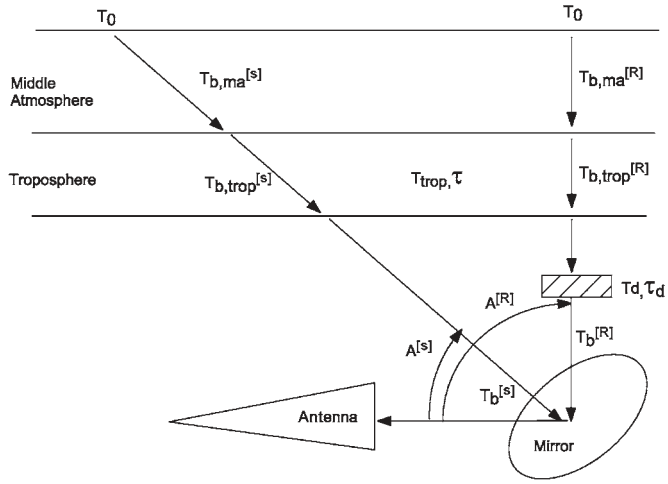

Fig. 5. Illustration of the decomposition of the balanced signal $T_{\rm b}^{[S-R]}$ into different contributions.

B. Correction for Tropospheric Attenuation and Elevation

From each calibrated balanced spectrum $T_{\rm a}^{[S-R]}$, the middle atmospheric contribution in zenith direction $T_{\rm b,ma}^{[z]}$ must be derived to be able to average the measurements made at different elevations and in different tropospheric conditions in order to improve signal-to-noise ratio.

By definition, $T_{\rm a}^{[S-R]}$ can be modeled as the difference between the signal beam $T_{\rm b}^{[S]}$ and the reference beam $T_{\rm b}^{[R]}$ contributions. As shown in Fig. 5, considering the troposphere as an isothermal layer of mean temperature $T_{\rm trop}$ and mean zenith opacity $\tau_{\rm trop}^{[z]}$, and based on (1), $T_{\rm b}^{[S]}$ and $T_{\rm b}^{[R]}$ can be modeled according to the cosmic background radiation T_0, the middle atmospheric emission $T_{\rm b,ma}$, and the physical temperature $T_{\rm d}$ and opacity $\tau_{\rm d}$ of the dielectric balance load in the reference beam

$$T_{\rm b}^{[S]} \approx \left(T_0 + T_{\rm b,ma}^{[S]}\right)e^{-\tau_{\rm trop}^{[z]}A^{[S]}} + T_{\rm trop}\left(1 - e^{-\tau_{\rm trop}^{[z]}A^{[S]}}\right) \tag{5}$$

$$T_{\rm b}^{[R]} \approx \left(T_0 + T_{\rm b,ma}^{[R]}\right)e^{-\tau_{\rm trop}^{[z]}A^{[R]}}e^{-\tau_{\rm d}} + T_{\rm trop}\left(1 - e^{-\tau_{\rm trop}^{[z]}A^{[R]}}\right)e^{-\tau_{\rm d}} + T_{\rm d}\left(1 - e^{-\tau_{\rm d}}\right) \tag{6}$$

where $A^{[S]}$ and $A^{[R]}$ are the tropospheric air mass factors (AMFs) in the $[S]$ and $[R]$ directions, respectively. The calculation of the AMF based on the elevation angle and antenna beam shape will be detailed in Section IV-A.

At 22.235 GHz, the middle atmospheric contribution accounts for less than 1% of the total atmospheric emission observed at any elevation from the ground [20]. By neglecting the middle atmospheric contribution, the opacity $\tau_{\rm d}$ of the dielectric balanced load can be estimated from (6) by

$$\tau_{\rm d} \approx -\ln\left(\frac{T_{\rm a}^{[R]} - T_{\rm d}}{T_0 e^{-\tau_{\rm trop}^{[z]}A^{[R]}} + T_{\rm trop}\left(1 - e^{-\tau_{\rm trop}^{[z]}A^{[R]}}\right) - T_{\rm d}}\right) \tag{7}$$

where $T_{\rm a}^{[R]}$ is the measured total power in the reference beam calibrated in brightness temperature by

$$T_{\rm a}^{[R]}(\nu) = \left(V_{\rm a}^{[R]}(\nu) - V_{\rm a}^{[\rm cold]}(\nu)\right)/G(\nu) + T_{\rm cold}. \quad (8)$$

The middle atmospheric emissions $T_{\rm b,ma}^{[S]}$ and $T_{\rm b,ma}^{[R]}$ in the $[S]$ and $[R]$ directions along the line of sight can be expressed based on the emission in the zenith direction $T_{\rm b,ma}^{[z]}$ by

$$T_{\rm b,ma}^{[S]} \approx T_{\rm b,ma}^{[z]} A_{\rm ma}^{[S]} \quad (9)$$

$$T_{\rm b,ma}^{[R]} \approx T_{\rm b,ma}^{[z]} A_{\rm ma}^{[R]} \quad (10)$$

where $A_{\rm ma}^{[S]}$ and $A_{\rm ma}^{[R]}$ are the middle atmospheric AMFs of the signal and reference beams, respectively.

By subtracting (6) from (5) and using (9) and (10), we can define the corrected spectrum $T_{\rm b,corr}$ as the relation between $T_{\rm a}^{[S-R]}$ and $T_{\rm b,ma}^{[z]}$

$$T_{\rm b,corr} = c_{\rm f} \cdot T_{\rm a}^{[S-R]} = T_{\rm b,ma}^{[z]} + T_{\rm b,res} \quad (11)$$

where $c_{\rm f}$ is the so-called correction factor given by

$$c_{\rm f} = \left(A_{\rm ma}^{[S]} e^{-\tau_{\rm trop}^{[z]} A^{[S]}} - A_{\rm ma}^{[R]} e^{-\tau_{\rm trop}^{[z]} A^{[R]}} e^{-\tau_{\rm d}}\right)^{-1} \quad (12)$$

and $T_{\rm b,res}$ is the frequency-dependent residual term having a null average value over the measurement bandwidth induced by the beam-switching method employed. It originates from the following: 1) a contribution from the tropospheric emission difference in the $[S]$ and $[R]$ directions, whose spectral shape can be modeled by a second-order polynomial function [21] and 2) the standing waves in the receiver that have a spectral periodicity related to the distances between reflecting obstacles in the instrument (see, e.g., [13]). We therefore use a sum of a second-order polynomial function and two sine functions to model $T_{\rm b,res}$.

From the corrected spectrum $T_{\rm b,corr}$, the inversion process (see Section V-A) actually retrieves the following: 1) the vertical middle atmospheric water vapor profile related to $T_{\rm b,ma}^{[z]}$ and 2) the parameters of the mathematical functions describing $T_{\rm b,res}$.

C. Filtering and Averaging

Calibrated and corrected spectra are filtered based on the variations (deviation from a running mean) in the signal averaged total power spectrum $T_{\rm a}^{[S]}$ and in the calibrated and corrected balanced spectrum $T_{\rm b,corr}$. Each individual $T_{\rm b,corr}$ spectrum corresponds to an effective integration time of 10 s. Data used for the retrieval of one vertical profile correspond to ∼1000 individual spectra (total effective integration time of ∼3 h), which are required to reduce the random noise level down to ∼10 mK based on the radiometer equation [22]. Fig. 6 shows the calibrated and corrected spectrum integrated over one day of measurement. For the retrieval of the middle atmospheric water vapor, only the 375-MHz band centered around the 22.235-GHz H_2O line is considered since the far wings of the spectrum are contaminated by the baseline structure and, therefore, cannot provide information on the vertical distribution of H_2O in the lower stratosphere.

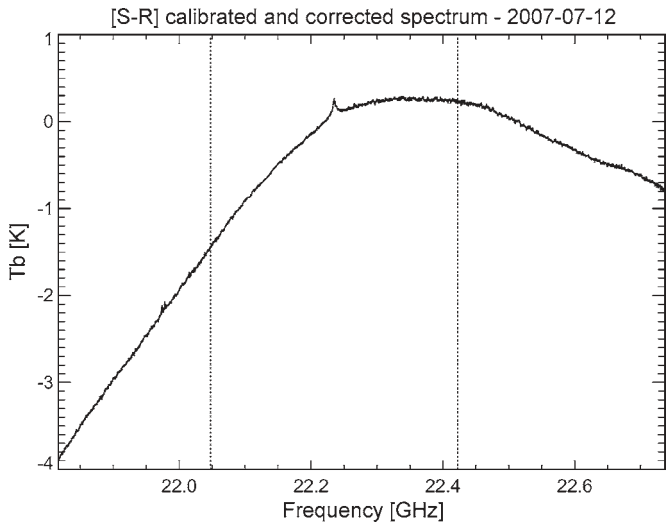

Fig. 6. Full bandwidth spectrum $T_{\rm b,corr}$ calibrated and corrected for tropospheric attenuation, which is daily averaged over July 12, 2007 (∼8000-s effective integration time). The retrieval process is actually performed within the spectral band delimited by the two vertical dotted lines (22.235 ± 0.185 GHz).

IV. Determination of Tropospheric Properties

In order to estimate the tropospheric properties needed to compute the correction factor $c_{\rm f}$ and to use the sky as a cold load, the tropospheric mean temperature $T_{\rm trop}$ and the opacity in zenith direction $\tau_{\rm trop}^{[z]}$ must be estimated. As explained in Section III-B, the middle atmospheric contribution accounts for less than 1% of the total atmospheric emission observed from the ground. With no dielectric balance load in the beam (elevation angle θ between 15° and 60°) and by neglecting the middle atmospheric contribution, the brightness temperature of the sky observed from the ground $T_{\rm b}(\theta)$ can be written from (5) as

$$T_{\rm b}(\theta) \approx T_0 e^{-A(\theta)\tau_{\rm trop}^{[z]}} + T_{\rm trop}(1 - e^{-A(\theta)\tau_{\rm trop}^{[z]}}) \quad (13)$$

where $A(\theta)$ is the AMF at elevation θ.

A. AMF

For ground-based instruments, the airmass factor is generally computed in a geometrical way as the ratio of the pathlength in the viewing direction upon the pathlength in the zenith direction. In the pencil-beam approximation [10], the AMF $A_{\rm pb}(\theta)$ takes into account the curvature of the Earth

$$A_{\rm pb}(\theta) = \frac{1 + z_{\rm ref}/R_{\rm e}}{\sqrt{\sin^2\theta + 2z_{\rm ref}/R_{\rm e} + (z_{\rm ref}/R_{\rm e})^2}} \quad (14)$$

where $z_{\rm ref}$ is the mean altitude of the considered layer. In this paper, we used $z_{\rm ref} = 4$ km for the tropospheric AMF and $z_{\rm ref} = 35$ km for the stratospheric AMF. $R_{\rm e}$ is the radius of the Earth ($R_{\rm e} = 6378$ km). However, this estimation introduces a

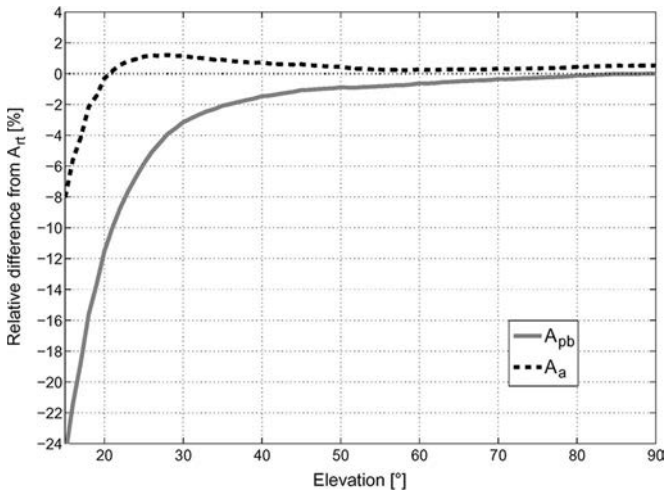

Fig. 7. Relative difference $(A_{\rm pb}(\theta) - A_{\rm rt}(\theta))/A_{\rm rt}(\theta)$ (solid line) and $(A_{\rm a}(\theta) - A_{\rm rt}(\theta))/A_{\rm rt}(\theta)$ (dashed line) versus elevation angle. A 12° FWHM Gaussian shape is assumed for the antenna beam.

strong bias when using a wide beamwidth antenna, particularly at low elevations, since the instrument couples radiation coming from other parts of the sky. To improve the calculation of the AMF, $A_{\rm pb}(\theta)$ is convolved with the instrument antenna pattern $F(\theta)$ to compute the antenna-corrected AMF $A_{\rm a}(\theta)$

$$A_{\rm a}(\theta) = \frac{\int_{-\pi}^{+\pi} A_{\rm pb}(\theta+\theta')F(\theta')d\theta'}{\int_{-\pi}^{+\pi} F(\theta')d\theta'}. \quad (15)$$

As suggested by Han [23], the AMF can also be defined as the ratio of the opacity $\tau(\theta)$ at a given elevation angle θ upon the opacity in the zenith direction $\tau^{[z]}$

$$A_{\rm rt}(\theta) = \tau(\theta)/\tau^{[z]}. \quad (16)$$

To compute the opacities in different viewing directions, we have used the generic Microwave Odin LIne Estimation and REtrieval (MOLIERE) radiative transfer and inversion tool that is fully described in Section V. MOLIERE simulates refraction, spherical geometry, antenna pattern, and ground emission. As an *a priori* information for the tropospheric temperature, pressure, and relative humidity vertical profiles, we have used one year of radiosoundings from the Mérignac Airport, France (44.8° N and 0.7° E), which is 200 km away from the instrument location.

Fig. 7 shows the relative difference between $A_{\rm rt}(\theta)$ and the other estimations, namely, $A_{\rm pb}(\theta)$ and $A_{\rm a}(\theta)$. A 12° FWHM Gaussian function is used to approximate the MobRa beamshape. At low elevation ($\theta \leq 15°$), a relative difference as high as 25% can be observed for $A_{\rm pb}(\theta)$ and 8% for $A_{\rm a}(\theta)$. This effect is mainly caused by ground emission, which is computed only in $A_{\rm rt}(\theta)$. Above 20° of elevation, $A_{\rm a}(\theta)$ shows very good agreement with $A_{\rm rt}(\theta)$ ($\leq 1\%$). The $A_{\rm pb}(\theta)$ estimation is valid within 1% only above 45° of elevation. This paper shows the following: 1) that it is important to take into account the antenna beamwidth in the computation of the AMF for MobRa and 2) that using elevation angles lower than 20° should be avoided in order to minimize ground effects.

B. Mean Tropospheric Temperature $T_{\rm trop}$

Several parameterizations have been developed to estimate $T_{\rm trop}$ from the ground temperature $T_{\rm ground}$. One of the most widely used is the one described in [23], which is a function of frequency and AMF but does not account for the beamshape. We have therefore used the radiative transfer model MOLIERE with the same *a priori* data and settings as the ones described in Section IV-A to compute the brightness temperature $T_{\rm b}$ and the opacity $\tau_{\rm trop}^{[z]}$ of the troposphere for different AMFs and then to estimate $\Delta T_{\rm rt}$, i.e., the difference between $T_{\rm ground}$ and $T_{\rm trop}$ versus elevation angle from (13).

The upper panel of Fig. 8 shows ΔT as calculated by the different methods. For AMFs$>$ 2, the difference between the output of the radiative transfer model $\Delta T_{\rm rt}$ and the Han method (an interpolated lookup table) [23] $\Delta T_{\rm Han}$ gradually increases to reach 10 K at AMF $= 3$. To assess the effect of the beamshape, a radiative transfer simulation with the pencil-beam approximation has been performed, yielding results that are very similar to the Han method.

The impact of the difference in $T_{\rm trop}$ on the calculation of other tropospheric parameters, namely, the opacity $\tau_{\rm trop}^{[z]}$ and the brightness temperature $T_{\rm b}$ when all the other variables of (13) are supposed to be known, is shown in the lower panel of Fig. 8. At low elevations (AMF $\geq$ 3), the difference on the calculation of $\tau_{\rm trop}^{[z]}$ can reach 0.015 Np, which corresponds to $\sim$15% of the opacity in clear sky conditions, and the difference on the estimation of $T_{\rm b}$ reaches 5 K, which represents $\sim$10% of the received brightness temperature in clear sky conditions. In our processing, a lookup table computed from MOLIERE simulations is used to estimate $T_{\rm trop}$ from the ground temperature and the elevation angle.

C. Opacity

To estimate the tropospheric opacity $\tau_{\rm trop}^{[z]}$, tipping curve measurements are performed after each calibration cycle, namely, every 15 $[S-R]$ measurements. The sky is scanned at eight different elevation angles between 60° and 25° (AMF ranging from 1.2 to 2.6, respectively). An iterative method introduced in [23] and adapted and validated by [24] is then used to estimate the opacity.

This method can be divided into five steps.

1) The sky brightness temperature at 60° of elevation is estimated from (12) with an initial value of the zenith opacity of 0.2.
2) The gain is computed by using the sky brightness temperature modeled in 1) as the cold load.
3) Tipping curve measurements are calibrated in brightness temperature from the new calculated gain.
4) The calibrated measurements are mapped into opacities in the line of sight.
5) The new zenith opacity is given by the slope of the linear fit of the line-of-sight opacities versus AMF.

The new zenith opacity is injected into step 1) until the offset at the origin of the line-of-sight opacities versus AMF fit is

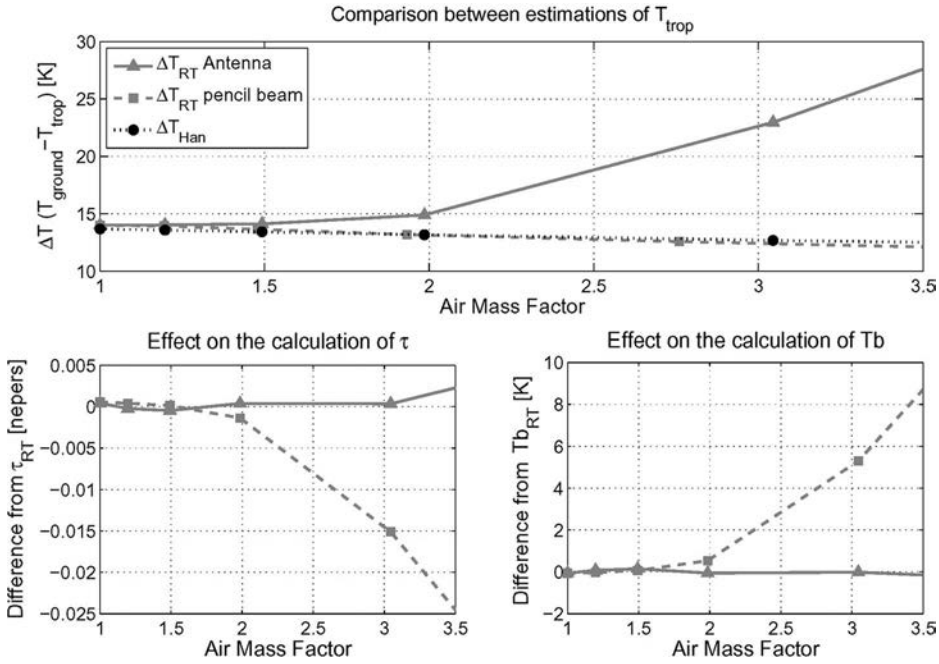

Fig. 8. Upper panel: Comparison of the estimation of ΔT versus AMF considering different methods, namely, radiative transfer with antenna radiation pattern (solid line and triangles), radiative transfer with pencil beam (dashed line and squares), and Han parameterization (dotted line and circles). Lower left panel: Impact of the difference in $T_{\rm trop}$ on the calculation of $\tau_{\rm trop}^{[z]}$. Lower right panel: Impact of the difference in $T_{\rm trop}$ on the calculation of $T_{\rm b}$.

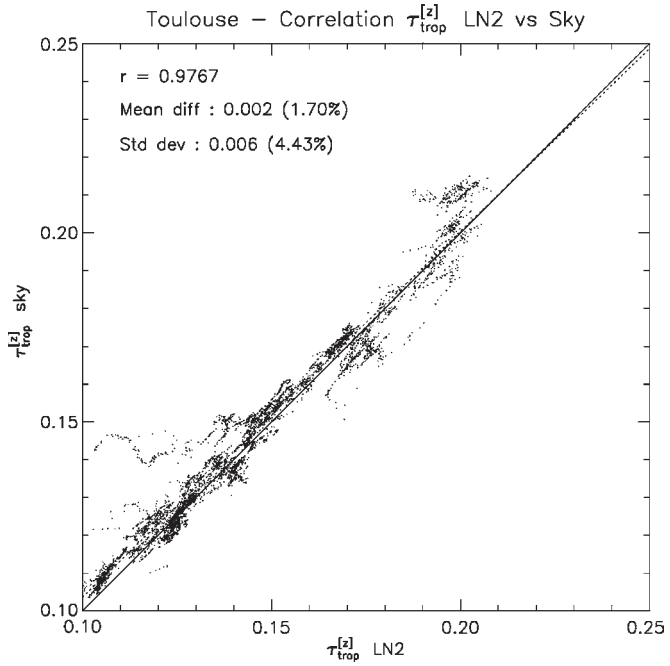

Fig. 9. Correlation between $\tau_{\rm trop}^{[z]}({\rm LN2})$ and $\tau_{\rm trop}^{[z]}({\rm Sky})$ estimated in Toulouse for the period from August 2 to 5, 2007.

smaller than 10^{-2}. The process usually converges after one or two iterations.

We compared the opacity derived from the LN2 calibration $\tau_{\rm trop}^{[z]}({\rm LN2})$ versus the opacity derived from the sky calibration $\tau_{\rm trop}^{[z]}({\rm Sky})$ for the period from August 2 to 5, 2007 (Fig. 9). The correlation factor r is $\sim$0.98, the mean difference is $\sim$1.70%, and the standard deviation is $\sim$4.5%.

D. Sky as a Cold Load

By knowing all the tropospheric parameters in (13), it is then possible to estimate the sky brightness temperature $T_{\rm b}$ and, therefore, to use the sky as a calibration load. To avoid interaction with the dielectric balance load and bias introduced by low elevation pointing, as for [13] and [14], we took an elevation value of 60° (AMF $= 1.2$) for this particular measurement.

In Fig. 10, we compared the value of $T_{\rm rec}$ estimated from August 2 to 5, 2007, by calibration methods using two different cold loads: LN2 and the sky at 60° of elevation. There is a good agreement between the two methods, with an average difference of $\sim$0.3 K ($\sim$0.25%) and a standard deviation of $\sim$6 K (3.5%).

Three artefacts, which are labeled 1–3, are shown in Fig. 8. The artefact labeled 2, which is occurring in the beginning of the local afternoon, is caused by a refill of the LN2 Dewar. The artefacts labeled 1 and 3 occurred at the same local time (August 3 and 4, 2007) a few minutes after sunrise. They are likely caused by a direct illumination of the hot load by the sun, producing differences between the physical temperature measured by the probe and the actual brightness temperature of the load. We are currently investigating other ways of positioning the temperature sensor in the hot load to avoid these fluctuations.

V. Preliminary Results

A. Forward Model and Retrieval Method

The MOLIERE code [25] was initially developed for the Odin satellite [5] and used in different ground-based projects, e.g., O_3 at 110 GHz [26] and ClO at 278 GHz [27]. The MOLIERE code is separated into a forward model and a retrieval code. The forward model includes modules for

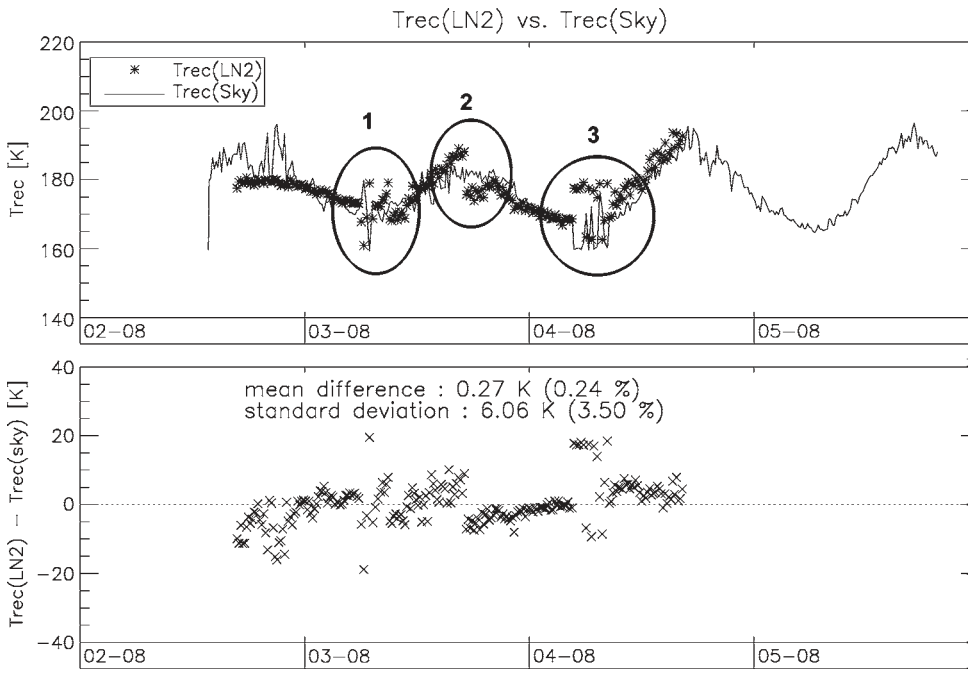

Fig. 10. Upper panel: Receiver temperature computed by using LN2 $T_{\rm rec}(\rm LN2)$ as a cold load (stars) and computed by using the sky $T_{\rm rec}(\rm sky)$ observed at an elevation of 60° (solid line) for the period from August 2 to 5, 2007. Three artefacts, which are labeled 1–3, have been circled (see text for details). Lower panel: Relative difference between $T_{\rm rec}(\rm LN2)$ and $T_{\rm rec}(\rm sky)$ for the same period.

spectroscopy, radiative transfer, and sensor characteristics (antenna, sideband filter, and spectrometer). It also includes different shapes of baseline undulations from cubic polynomial to sine functions. The retrieval code is based upon the optimal estimation method [28] and, coupled with the forward model, allows nonlinear retrievals based on a Newton Levenberg–Marquardt iteration scheme. An additional noise parameter can also be added to the random radiometric noise in order to cope with any spurious noise that cannot be fitted by an algebraic mathematical function.

Spectroscopic line parameters for the line-by-line calculations have been taken from the Verdandi database (http://www.rss.chalmers.se/gem/Research/verdandi.html), which merges frequencies, line intensities, and lower state energies from the JPL catalogue [29] with pressure broadening parameters from the HITRAN compilation [30]. Only the $6_{16}-5_{23}$ transition at 22.235 GHz is considered in this paper.

In this paper, the *a priori* information on H_2O, temperature, pressure, and altitude has been taken from the European Center for Medium-Range Weather Forecasts analysis. The *a priori* error on H_2O profiles has been set to 25% of the *a priori* mixing ratios, and a diagonal covariance matrix has been built. The additional noise parameter has been set to 5 mK. The maximum number of iterations has been set to ten.

As explained in Section III-B, the residual contribution $T_{\rm b,res}$ can be decomposed into the following two parts: 1) the second-order polynomial function describing the troposphere residual contribution and 2) the two sine functions related to reflections within the instrument. All the parameters of the baseline are retrieved during the inversion process. However, because of their different natures, two methods have been used to estimate the baseline *a priori* values and associated errors which will then remain the same for the whole measurement period.

First, in the case of the polynomial function, for a given site and a given measurement period, the *a priori* and error of the coefficients should be as close as possible to their mean value and natural variability, respectively. Therefore, we performed a two-step inversion. The first step consists in a retrieval of the coefficients of the polynomial function for each day of the whole period with *a priori* values set to zero and a large associated error. In the second step, the average and standard deviation of the retrieved parameters are then calculated over the whole period and used as *a priori* and errors, respectively, to actually perform daily inversions.

Second, in the case of the sine functions, we used another approach. On the one hand, it is difficult to estimate the frequency of a sine function within the inversion process since it is highly nonlinear. On the other hand, the frequency induced by the physical length scales of the instrument does not change much with time. Therefore, as a first step, we performed a study to determine the frequencies of the sine functions, consisting in a Fourier transform analysis of the measured spectra anomaly [20]. Values of 200 and 150 MHz have been found, with associated amplitudes of 30 $\pm$ 5 and 13 $\pm$ 5 mK, respectively. Then, in the second step, these values are used as *a priori* for the frequency of the sine functions, with associated errors set to zero, so that only the phase and the amplitude of the sine functions are actually estimated in the daily inversions.

B. Spectra

The instrument has performed 20 days of measurements in its optimal configuration during summer 2007 on the terrace of the Laboratoire d'Aérologie, Toulouse (45° N, 2.5° E, and 150 m a.s.l.). Fig. 11 (top) shows a typical daily averaged spectrum as measured on July 12, 2007. Only the bandwidth

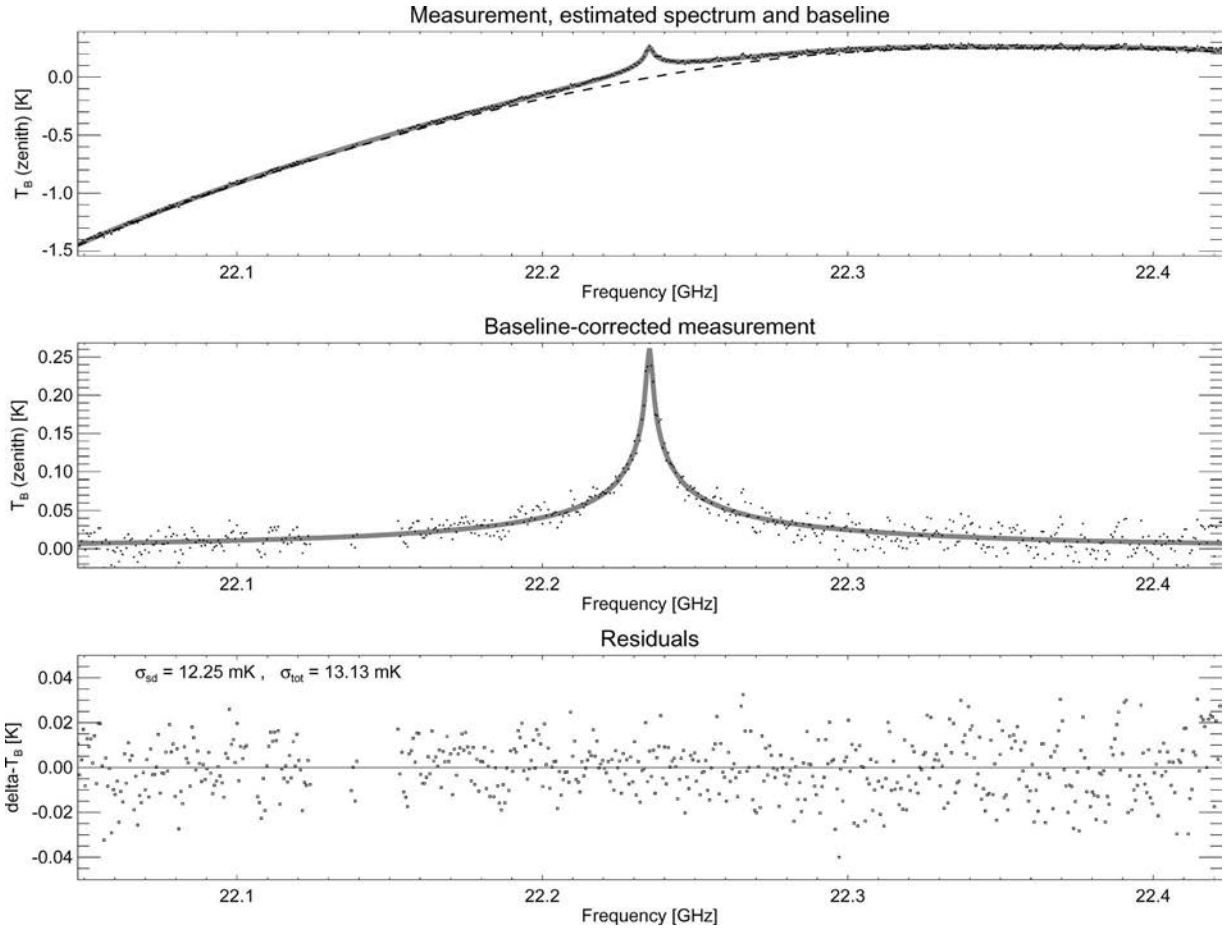

Fig. 11. Twenty-four-hour averaged spectrum within 375 MHz centered around the 22.235-GHz transition line as measured by the MobRa instrument over Toulouse, France, on July 12, 2007. Top: Calibrated and troposphere-corrected spectrum (dots), estimated by MOLIERE (thick gray line), and estimated $T_{\mathrm{b,res}}$ (dashed). Middle: Middle atmospheric emission $T_{\mathrm{b,corr}} - T_{\mathrm{b,res}}$ (dots) and estimated by MOLIERE (thick gray line). Bottom: Residuals.

used for retrieval is shown (375 MHz around the line center). The integration time is about 8000 s. The estimated $T_{\mathrm{b,res}}$ is shown as the dashed line. The estimated middle atmospheric emission in the zenith direction $T_{\mathrm{b,ma}}^{[z]} = T_{\mathrm{b,corr}} - T_{\mathrm{b,res}}$ from the measured and modeled spectra is shown in Fig. 11 (center). The standard deviation of the residuals (Fig. 11, bottom) is $\sim$12 mK, whereas the total instrumental noise (average thermal noise and additional random noise) is about 13 mK. Thus, in terms of residuals, the retrievals can be considered as good.

C. Vertical Profiles

The width at half-maximum of the averaging kernels provided by the optimal estimation theory can be considered as representative of the vertical resolution of the measurements. The sum of the elements of each averaging kernel (the measurement response) is an indication of the information provided by the measurement upon the *a priori* information. The optimal vertical domain where a meaningful information can be retrieved is estimated by a measurement response greater than 0.75, which means that the *a priori* information contaminates the retrieval by less than 25%.

The vertical profile is estimated after five iterations (Fig. 12, left) from 25 to 55 km, with a vertical resolution between $\sim$10 and $\sim$20 km increasing with height (Fig. 12, right). The measurement error is $\sim$0.8 ppmv ($\sim$15%). The normalized χ^2 (chi-square) indicates a good retrieval process when close to one. The calculated normalized χ^2 is 0.86 in our case, underlying that retrieval parameters (e.g., additional noise, *a priori* covariance matrices, etc.) still need to be optimally tuned. The number of independent vertical elements of information, which is calculated as the trace of the averaging kernel matrix, is 2.4.

D. Preliminary Validation

The MLS instrument aboard the Aura satellite has been launched in 2003 and has been providing H_2O validated profiles since then [6]. We used MLS H_2O data version 2.2 to validate our measurements. Every daily vertical profile from MobRa is compared with an average of all the profiles from MLS measured in time coincidence of $\pm$12 h around the daily bin and in spatial coincidence within $\pm 2^\circ$ in latitude and $\pm 5^\circ$ in longitude around the location of MobRa. This corresponds to approximately five MLS profiles per day. The vertical resolution of MLS profiles (2–5 km) is higher than the vertical resolution of MobRa profiles (10–20 km). Therefore, the MLS profiles have been convolved by MobRa averaging kernel matrix and *a priori* vertical profiles in order to match the resolution of the ground-based instrument and to account for the *a priori* contribution in the retrieval (see, e.g., [27] for

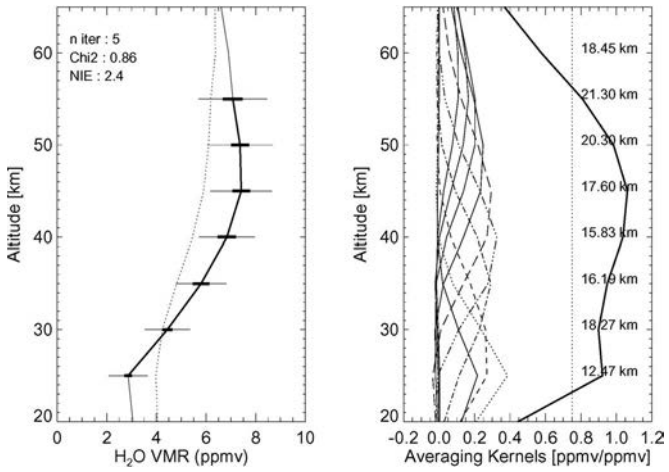

Fig. 12. (Left) Vertical H_2O profiles for July 12, 2007. *A priori* (dots) and estimated (solid) profiles. The thin horizontal lines correspond to the total error, and the horizontal thick lines correspond to the measurement error within the optimal retrieval domain (i.e., measurement response greater than 0.75). (Right) H_2O averaging kernels, measurement response (thick solid line), and vertical resolution associated to each averaging kernel (in kilometers). The vertical dotted line represents the 0.75 measurement response.

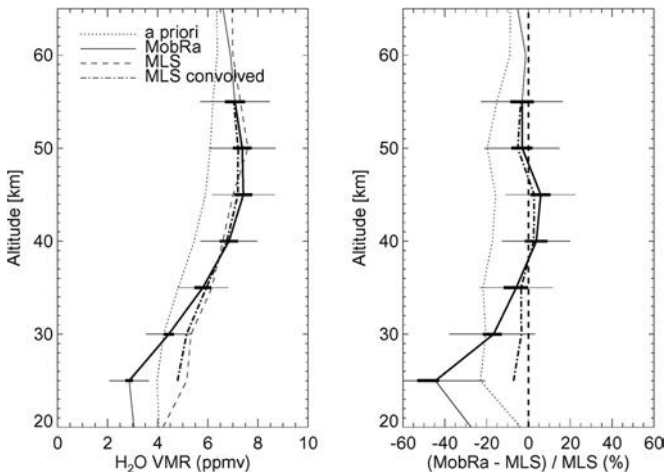

Fig. 13. (Left) H_2O vertical profiles and (right) relative difference from MLS for July 12, 2007: *A priori* (dots), MobRa (solid), MLS (dashed), and MLS convolved with the averaging kernels of MobRa in order to match the ground-based instrument vertical resolution (dashed–dot).

a detailed description of the convolution procedure). Fig. 13 (left) shows the vertical profiles for July 12, 2007, from MobRa, MLS (four averaged profiles), and MLS convolved with MobRa averaging kernels, as well as the *a priori* profile. The right panel shows the relative difference from the MLS profiles. A good agreement ($\pm 5\%$) can be observed between MobRa and MLS in the altitude range of 35–55 km. Below 35 km, MobRa starts to underestimate H_2O compared with MLS. The difference between MobRa and MLS reaches about -20% and -40% at 30 and 25 km, respectively, reducing down to about -15% and -30%, respectively, when compared with the MLS convolved vertical profiles.

The difference between MobRa and MLS in the lower stratosphere is likely to be induced by the instrumental baseline contamination. A better characterization of $T_{\mathrm{b,res}}$ and the use of a phase shifter properly tuned to minimize the standing waves in the receiver [14] will probably improve the retrieval of H_2O in the lower stratosphere.

VI. Conclusion and Further Work

A new compact, mobile, and automated radiometer (MobRa) has been developed for measuring water vapor in the middle atmosphere by detecting the 22.235-GHz emission line. The bias caused by the wide beamwidth antenna is corrected by including the antenna radiation pattern in the calculation of elevation-dependent parameters. Tipping curve measurements are used to estimate the opacity of the troposphere and to calculate the brightness temperature of the sky, which can, in turn, be used as a cold load. A comparison against LN2 calibration shows good agreement when considering T_{rec} (relative absolute difference $<1\%$). First daily-averaged measured spectra show very promising moderate baseline undulations. Retrievals of middle atmospheric H_2O have been achieved, giving vertical profiles from 25 to 55 km with a measurement error of $\sim$0.8 ppmv ($\sim$15%) and a vertical resolution ranging from 10 to 20 km, increasing with height. Further work on baseline minimization and characterization will help enlarge the retrieval range toward the lower stratosphere. Preliminary validations with Aura/MLS show a good agreement ($\sim$5%) in the 35–55-km altitude range, but a strong negative bias appears at lower altitudes (up to about -30% at 25 km), which is probably induced by an instrumental baseline contamination. Further long-term validation of the H_2O retrievals against model outputs and measurements from spaceborne and ground-based instruments are required to assess the quality of the measurements so that the MobRa radiometer can be part of NDACC.

Acknowledgment

The authors would like to thank the Centre National de la Recherche Scientifique and the Centre National d'Etudes Spatiales for funding the Ph.D. thesis of E. Motte; the Institut National des Sciences de l'Univers and the Observatoire Midi-Pyrénées for partly funding the technical work on MobRa; J. de La Noë for initiating this project; and J. Urban for the initial work on the instrument and the work on the MOLIERE tools in Bordeaux, France. The authors would also like to thank H. Sauvageot of the Laboratoire d'Aérologie, France, for the helpful discussions; the Office National d'Etudes et de Recherche Aérospatiale for providing measurement facilities in Toulouse, France; Prof. N. Kämpfer and A. Haefle of the University of Bern, Switzerland, for their expertise and welcoming in Bern for an intercomparison campaign during summer 2006; and the IEEE reviewers for their helpful comments.

References

[1] S. J. Oltmans and D. J. Hofmann, "Increase in lower-stratospheric water vapour at a mid-latitude northern hemisphere site," *Nature*, vol. 374, no. 6518, pp. 146–149, Mar. 1995.

[2] K. H. Rosenlof *et al.*, "Stratospheric water vapor increases over the past half-century," *Geophys. Res. Lett.*, vol. 28, no. 7, pp. 1195–1198, Apr. 2001.

[3] W. J. Randel, F. Wu, H. Vömel, G. E. Nedoluha, and P. Forster, "Decreases in stratospheric water vapor after 2001: Links to changes in the tropical tropopause and the Brewer–Dobson circulation," *J. Geophys. Res.*, vol. 111, no. 10, p. 12 312, Jun. 2006.

[4] M. Scherer, H. Vömel, S. Fueglistaler, S. J. Oltmans, and J. Staehelin, "Trends and variability of midlatitude stratospheric water vapour deduced from the re-evaluated boulder balloon series and haloe," *Atmos. Chem. Phys. Discuss.*, vol. 7, no. 5, pp. 14 511–14 542, 2007.
[5] D. Murtagh *et al.*, "Review: An overview of the Odin atmospheric mission," *Can. J. Phys.*, vol. 80, pp. 309–319, Apr. 2002.
[6] L. Froidevaux *et al.*, "Early validation analyses of atmospheric profiles from EOS MLS on the Aura satellite," *IEEE Trans. Geosci. Remote Sens.*, vol. 44, no. 5, pp. 1106–1121, May 2006.
[7] B. Carli *et al.*, "First results of MIPAS/ENVISAT with operational level 2 code," *Adv. Space Res.*, vol. 33, no. 7, pp. 1012–1019, 2004.
[8] J. A. Lerner, E. Weisz, and G. Kirchengast, "Temperature and humidity retrieval from simulated infrared atmospheric sounding interferometer (IASI) measurements," *J. Geophys. Res.*, vol. 107, no. D14, 4189, Jul. 2002.
[9] H. E. Radford *et al.*, "Mesospheric water vapor measured from ground-based microwave observations," *J. Geophys. Res.*, vol. 82, no. 11, pp. 472–478, Feb. 1977.
[10] A. Parrish, R. L. Dezafra, P. M. Solomon, and J. W. Barrett, "A ground-based technique for millimeter wave spectroscopic observations of stratospheric trace constituents," *Radio Sci.*, vol. 23, no. 2, pp. 106–118, Apr. 1988.
[11] G. E. Nedoluha *et al.*, "Ground-based measurements of water vapor in the middle atmosphere," *J. Geophys. Res.*, vol. 100, no. D2, pp. 2927–2939, Feb. 1995.
[12] D. L. Thacker *et al.*, "Ground-based sensing of water vapor in the stratosphere and mesosphere," *IEEE Trans. Instrum. Meas.*, vol. 44, no. 2, pp. 355–359, Apr. 1995.
[13] P. Forkman, P. Eriksson, and A. Winnberg, "The 22 GHz radio-aeronomy receiver at Onsala Space Observatory," *J. Quant. Spectrosc. Radiat. Transf.*, vol. 77, no. 1, pp. 23–42, Feb. 2003.
[14] B. Deuber, N. Kämpfer, and D. G. Feist, "A new 22-GHz radiometer for middle atmospheric water vapor profile measurements," *IEEE Trans. Geosci. Remote Sens.*, vol. 42, no. 5, pp. 974–984, May 2004.
[15] S. Golchert, *Radiometer for atmospheric measurements web site*, 2006. [Online]. Available: http://www.iup.uni-bremen.de/ram/ramtext.html.
[16] NDACC, *NDACC web site*, 2007. [Online]. Available: http://www.ndsc.ncep.noaa.gov.
[17] M.A. Janssen, Ed., *Atmospheric Remote Sensing by Microwave Radiometry*. New York: Wiley, 1993.
[18] S. Chandrasekhar, *Radiative Transfer*. New York: Dover, 1960.
[19] F. T. Ulaby, R. K. Moore, and A. F. Kung, *Microwave Remote Sensing: Active and Passive*, vol. 1. Norwood, MA: Artech House, 1981.
[20] E. Motte, "MobRa, un radiomètre micro-onde mobile pour la mesure de la vapeur d'eau dans la moyenne atmosphère," Ph.D. dissertation, Univ. Toulouse III, Toulouse, France, 2008.
[21] A. Haefele, "Atmosphärische wasserdampfprofile von 0–60 km aus optimierter kombination von mikrowellendaten und ballonsondierungen," M.S. thesis, Philosophisch-Naturwissenschaftliche Fakultät, Univ. Bern, Bern, Switzerland, Jan. 2005.
[22] J. Kraus, "Radio astronomy," in *Cygnus Quasar Books*. New York: McGraw-Hill, 1966.
[23] Y. Han and E. R. Westwater, "Analysis and improvement of tipping calibration for ground-based microwave radiometers," *IEEE Trans. Geosci. Remote Sens.*, vol. 38, no. 3, pp. 1260–1276, May 2000.
[24] A. Haefele, "On tipping curve calibration and tropospheric correction for a 22 GHz spectro-radiometer," Inst. angewandte Phys., Univ. Bern, Bern, Switzerland, IAP Res. Rep., Jan. 2008.
[25] J. Urban *et al.*, "Moliere (v5): A versatile forward- and inversion model for the millimeter and sub-millimeter wavelength range," *J. Quant. Spectrosc. Radiat. Transf.*, vol. 83, no. 3/4, pp. 529–554, Feb. 2003.
[26] N. Schneider, O. Lezeaux, J. de La Noë, J. Urban, and P. Ricaud, "Validation of ground-based observations of stratomesospheric ozone," *J. Geophys. Res.*, vol. 108, no. D17, 4540, Sep. 2003.
[27] P. Ricaud, P. Baron, and J. La Noë, "Quality assessment of ground-based microwave measurements of chlorine monoxide, ozone, and nitrogen dioxide from the NDSC radiometer at the Plateau de Bure," *Ann. Geophys.*, vol. 22, no. 6, pp. 1903–1915, 2004.
[28] C. D. Rodgers, *Inverse Methods for Atmospheric Sounding: Theory and Practice*, 1st ed. Singapore: World Scientific, 2000.
[29] H. M. Pickett *et al.*, "Submillimeter, millimeter, and microwave spectral line catalog," *J. Quant. Spectrosc. Radiat. Transf.*, vol. 60, no. 5, pp. 883–890, Nov. 1998.
[30] L. Rothman *et al.*, "The HITRAN 2004 molecular spectroscopic database," *J. Quant. Spectrosc. Radiat. Transf.*, vol. 96, no. 2, pp. 139–204, Dec. 2005.